Predicting and Probing the Local Temperature Rise Around Plasmonic Core–Shell Nanoparticles to Study Thermally Activated Processes

Mertens, Johannes C.J.; Spitzbarth, Benjamin; Eelkema, Rienk; Hunger, Johannes; van der Veen, Monique A.

DOI
10.1002/cplu.202400134

Publication date
2024

Document Version
Final published version

Published in
ChemPlusChem

ChemPlusChem

Research Article
doi.org/10.1002/cplu.202400134

Chemistry Europe
European Chemical Societies Publishing

www.chempluschem.org

Predicting and Probing the Local Temperature Rise Around Plasmonic Core–Shell Nanoparticles to Study Thermally Activated Processes

Johannes C. J. Mertens,[a] Benjamin Spitzbarth,[a] Rienk Eelkema,[a] Johannes Hunger,[b] and Monique A. van der Veen*[a]

Ultrafast spectroscopy can be used to study dynamic processes on femtosecond to nanosecond timescales, but is typically used for photoinduced processes. Several materials can induce ultrafast temperature rises upon absorption of femtosecond laser pulses, in principle allowing to study thermally activated processes, such as (catalytic) reactions, phase transitions, and conformational changes. Gold–silica core–shell nanoparticles are particularly interesting for this, as they can be used in a wide range of media and are chemically inert. Here we computationally model the temporal and spatial temperature profiles of gold nanoparticles with and without silica shell in liquid and gas media. Fast rises in temperature within tens of picoseconds are always observed. This is fast enough to study many of the aforementioned processes. We also validate our results experimentally using a poly(urethane-urea) exhibiting a temperature-dependent hydrogen bonding network, which shows local temperatures above 90 °C are reached on this timescale. Moreover, this experiment shows the hydrogen bond breaking in such polymers occurs within tens of picoseconds.

Introduction

Ultrafast pump–probe spectroscopy is an important technique used to directly probe ultrafast ((sub)femtosecond to nanosecond) dynamics. Originally, it was used in photochemistry to study photoactivated processes and directly observe photoexcited states, charge transfer, and short-lived reaction intermediates.[1] In this technique, two pulses of light are used: first a pump pulse that collectively starts a large number of the same processes at the same time, and subsequently a probe pulse to detect the progress of these chemical processes. By varying the time between these pulses, a chemical process can be followed over time, and due to the collective starting, species that normally elude detection can be measured.[2] Using femtosecond laser pulses, this allows for a subpicosecond time resolution, which can even be pushed to the subfemtosecond domain when using attosecond laser pulses.[3–7] On this timescale, a variety of processes can be studied, such as electron dynamics, nuclear dynamics such as reactions or conformational changes, and thermal transport processes.[7,8]

Since a light pulse is used as pump, this technique is mostly limited to photoactivated processes. Various other techniques can be applied to non-photoactivated processes, but these lack the time resolution of pump–probe spectroscopy. For example, reactions can be studied by using a pulsed stream of molecules delivering one of the reactants as the pump. The time resolution is however limited to the microsecond timescale.[9] Techniques like operando spectroscopy in heterogeneous catalysis are limited by the velocity by which concentrations of reactants or the temperature can be increased. Therefore, these techniques are generally limited to the millisecond regime and only longer lived intermediates can be observed.[10–12] Reaction monitoring by mass spectrometry on microdroplets allows for capturing intermediates with microsecond lifetimes and time dynamics on a similar scale.[13–15] Phase transitions have been studied on the submicrosecond timescale using indirectly heated switches, which provide fast electrical heating of hundreds of degrees.[16] However, none of these techniques extend to nanosecond or picosecond timescales.

A more general approach is to use an ultrafast temperature jump induced by the optical pump pulse, such that pump–probe spectroscopy can also be used to study processes that are thermally initiated. An important class is that of reactions, since most reactions can be thermally activated, but other processes such as phase transitions, mass transport, and reactive crystallization are thermally initiated as well. Various approaches to achieve this have been used in literature, generally by employing a light pulse that is absorbed and converted into thermal energy. This usually results in rapid temperature rises on the order of 10 °C, but some allow for greater temperature jumps. For example, direct heating of a

[a] J. C. J. Mertens, Dr. B. Spitzbarth, Dr. R. Eelkema, Dr. M. A. van der Veen
Department of Chemical Engineering,
Delft University of Technology,
Van der Maasweg 9, 2629 HZ Delft, The Netherlands
E-mail: m.a.vanderveen@tudelft.nl

[b] Dr. J. Hunger
Max Planck Institute for Polymer Research,
Ackermannweg 10, 55128 Mainz, Germany

Supporting information for this article is available on the WWW under https://doi.org/10.1002/cplu.202400134

catalyst supported by alumina by light has been used in the more traditional step-scan Fourier-transform infrared (FTIR) spectroscopy to measure on the submicrosecond timescale, allowing to elucidate an intermediate with a 2 μs lifetime.[17] In water, using the pump–probe scheme, various types of light have been used for ultrafast temperature rises. Terahertz pulses allow for temperature rises of hundreds of degrees of water and its solutes within a picosecond.[18,19] Nanosecond far-infrared pulses have been used to excite hydroxyl vibrations in water to increase the temperature, but this was only used on the millisecond timescale.[20] Using near-infrared hydroxyl vibrations, this was achieved on the picosecond timescale.[21,22] As an alternative not limited to aqueous solutions, organic dyes can be employed that result in heating on the picosecond timescale. This can be done both via pump pulses in the visible[23] or in the near-infrared,[24] where a larger temperature jump of around 100 °C was achieved. This method is applicable to a wide range of media, yet has a few disadvantages limiting its applicability. Organic dyes have a large amount of vibrations in the mid-infrared range, making dye heating less appropriate for use with mid-infrared probes. Moreover, the dyes may not be chemically inert which can interfere with the phenomenon to be probed, *e.g.* when studying chemical reactions.

In order to make the ultrafast temperature jump more generally applicable, we want to employ nanoheaters that can achieve high temperature rises in various environments, that have no specific vibrations in the mid-infrared range and that are chemically inert. Plasmonic nanoparticles show a photothermal effect with which they convert light into heat,[25] can be encapsulated in inert shells like silica,[26] and can be deployed in a variety of environments,[25–27] making them prime candidates for nanoheaters. When plasmonic nanoparticles are illuminated by a femtosecond light pulse, energy is absorbed due to local surface plasmon resonance. This quickly generates out-of-equilibrium hot carriers, which are thermalized through electron–electron scattering within a picosecond. The raised electron temperature then leads to an increase of the lattice temperature of the nanoparticle through electron–phonon scattering on the scale of multiple picoseconds. Subsequently, this heat is dissipated from the nanoparticle to its environment.[25] It has even been proposed that employing this photothermal heating effect via repetitive ultrashort light pulses can increase thermocatalytic conversion.[28] This heating is spatially confined to near the nanoparticles when compared to techniques directly heating the solvent. While this means a smaller volume is heated, this can be compensated by system design and a larger penetration depth of the light. Additionally, this facilitates heat dissipation between pump pulses and thus reduces heat accumulation, allowing for higher pulse energies.

The heating provided by plasmonic nanoparticles after femtosecond-pulsed illumination has been studied both computationally and experimentally in literature, most of which focusing on aqueous media. Both approaches show for gold nanoparticles that those with a diameter of approximately effect the largest temperature increase in their surroundings: this is an optimum because while larger nanoparticles are favored because they have less surface area with respect to their volume, this only holds while their absorption cross section scales linearly to their volume, which is no longer the case when nanoparticles get above a certain size.[29,30] The studies on the time in which these temperatures are reached are mostly computational, and study how this depends on the size of the nanoparticle. For small gold nanospheres (10 nm diameter) the maximum temperature of the directly surrounding water is reached in tens of ps, while for larger gold nanospheres (200 nm diameter) this happens in hundreds of ps.[30] Gold nanorods show similar time dynamics, and can be approximated with nanospheres with some loss of accuracy.[31] In contrast to metals such as gold, transition metal nitrides have much faster electron–phonon coupling, resulting in a conversion of absorbed photons into heat in less than 100 fs.[32] The dissipation of heat to the surrounding water happened gradually on the order of magnitude of 100 ps, similar to gold nanoparticles. Yet, the faster electron–phonon coupling compared to gold holds promise for a faster initial temperature rise of the environment.[32] Mid-infrared transient absorption (MIR-TA) spectroscopy has been used to measure time dynamics of the temperature of the medium after femtosecond-pulsed illumination, specifically for gold nanorods in water. The time constant with which bare nanorods heat water was shown to be 350 ps.[33]

Bare plasmonic nanoparticles also influence their surroundings in addition to providing heat. During excitation of the nanoparticle by the pump pulse, the electromagnetic field near the nanoparticle is greatly amplified, which can enhance nearby optical processes and drive photochemical reactions.[25,36] Additionally, out-of-equilibrium hot carriers are generated after excitation, which can inject into molecules or materials in contact with the nanoparticle and mediate reactions in these materials.[25,36] While these effects are of great relevance for plasmon-mediated photocatalysis, plasmonic nanoparticles used for ultrafast heating should be designed to minimize these effects. This can be done by encapsulated them in an inert shell, such as a silica or alumina shell. This prevents the injection of hot carriers and reduces or removes the enhanced electric field outside the shell, allowing only the photothermal effect to be studied (Figure 1). This is similar to the shell-isolated nanoparticles used in shell-isolated nanoparticle-enhanced Raman spectroscopy (SHINERS).[26]

Inert shells also increase the thermal stability of nanoparticles[37,38] but can slow down heat transfer, since electric insulators are generally poor heat conductors. In contrast to previous work, we here therefore computationally study the effect of inert shells on the heat transfer of plasmonic nanoparticles to their surroundings. For this, we use gold–silica core–shell nanoparticles, which are often used in SHINERS and other ultrafast plasmonic applications.[25,26,37–40] We consider these in a range of media, namely air, water and organic materials, to evaluate the expected temporal and spatial temperature profiles when using gold–silica core–shell nanoparticles as nanoheaters in different pump–probe spectroscopy experiments. Additionally, we experimentally verify the temperature rise for gold–silica core–shell nanoparticles embedded in an organic material using MIR-TA. We chose a poly(urethane-

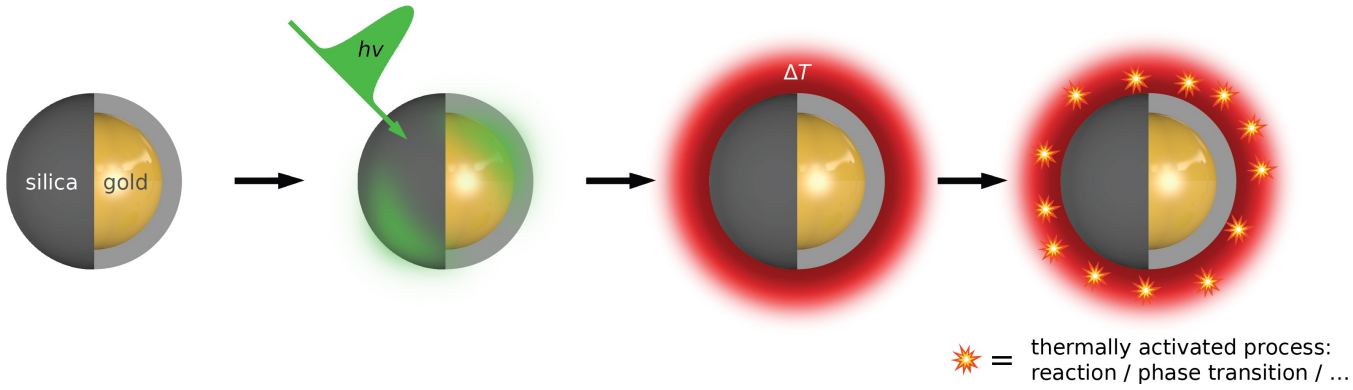

Figure 1. Depiction of the processes a gold–silica core–shell nanoparticle undergoes after excitation by a femtosecond light pulse. First there is a local electric field during the pulse, and hot electrons shortly thereafter. Due to electron–phonon scattering the nanoparticle heats up, and with it its surroundings. The high local temperatures generated can result in the thermal activation of processes near the nanoparticle, depending on the material surrounding the nanoparticle.

urea) (PUU) as the infrared spectrum of this polymer exhibits non-linear temperature dependence. This allows us to determine whether fast and high temperature rises around these core–shell nanoparticles indeed do occur experimentally, and whether the technique can be used to follow thermally activated processes.

Modeling Framework

To study the heat transfer from plasmonic core–shell nanoparticles to their environment, we use a model based on the work of Baffou et al.[41] and Metwally et al.[30] The original model was limited to gold nanoparticles in water. We extend the model in this work to more materials and, most importantly, more layers to allow for core–shell nanoparticles. In this section the model will be briefly described, a more complete description can be found in section S1. In this model we consider a single spherical nanoparticle and assume the nanoparticle and its environment can be treated as spherically symmetrical, *i.e.* each point at distance r from the center has identical material properties and an identical temperature. This allows us to neglect collective heating effects and spatially discretize the nanoparticle into layers (Figure 2a) where we can assume that each layer is uniform and can be described by a single temperature.

Since we base the model on Fourier's law,[42] the heat transfer within a material is defined by the partial differential equation (PDE):

$$\rho_i c_i \frac{\partial T(r,t)}{\partial t} = \kappa_i \vec{\nabla}^2 T(r,t) + p(r,t) \tag{1}$$

where the temperature T depends on the material properties density ρ, specific heat capacity c and heat conductivity κ of the material i. We assume these to be temperature-independent for the range reached during the simulation (Table 1). The production function p is the heat generation in the core of the plasmonic nanoparticle due to light illumination. For nanospheres, Mie theory[43,44] can be used with literature optical constants[45] to analytically calculate the total absorbed energy, which is distributed evenly over the core.[46] Since a femtosecond excitation pulse is short in comparison to the electron–phonon scattering transferring the energy absorbed by the electrons to thermal energy, the time dynamics under femtosecond excitation are determined by the latter.[30] It therefore follows an exponential decay like:

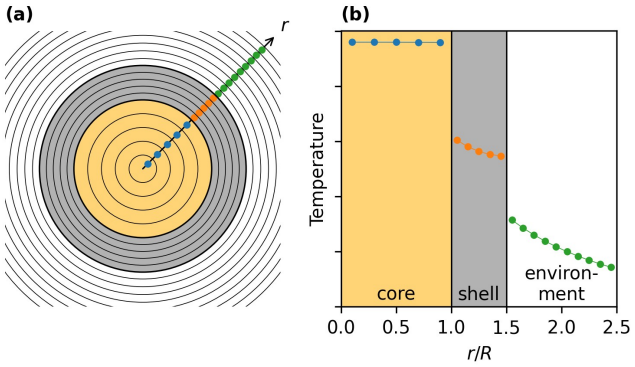

Figure 2. Depiction of (a) nanoparticle and spatial discretization in model and (b) resulting temperature profiles, showcasing temperature jumps due to interfacial conductance.

$$p(r,t) \propto \begin{cases} e^{-\frac{t}{\tau_{e-p}}} & \text{for } r \leq R \text{ (inside of core) and} \\ 0 & \text{for } r > R \text{ (outside of core)} \end{cases} \tag{2}$$

with the electron–phonon scattering time constant τ_{e-p} and nanoparticle core radius R.

With this, the heat transfer within materials is sufficiently defined. For the heat transfer between layers of different materials, we need to take the interfacial conductance G, also known as the Kapitza conductance, into account.[30] A finite G results in a temperature discontinuity described by:

Table 1. Material properties used in the model: the heat conductivity κ, density ρ, and specific heat capacity c, as well as the properties derived from these: the volumetric heat capacity ρc and thermal diffusivity $\alpha = \frac{\kappa}{\rho c}$.

Material	κ (W m^{-1} K^{-1})	ρ (kg m^{-3})	c (J kg^{-1} K^{-1})	ρc (kJ m^{-3} K^{-1})	α (mm^2 s^{-1})
Gold[34]	317	19 300	129	2490	127
Silica[34]	1.4	2196	739	1623	0.863
Water[34]	0.606 52	997	4181	4169	0.146
Air[34]	0.026 38	1.161	1007	1.169	22.6
Ethanol[34]	0.167	789.3	2438	1924	0.0868
Polyurethane[35]	0.19	1100	2500	2750	0.069

$$\kappa_i \left.\frac{\partial T(r,t)}{\partial r}\right|_{r_i} = G_{ij}\left(T(r_i,t) - T(r_j,t)\right) = \kappa_j \left.\frac{\partial T(r,t)}{\partial r}\right|_{r_j} \quad (3)$$

and also depicted in Figure 2b. The values used for the various interfaces are shown in Table 2.

The system of PDEs can be transformed to a system of ordinary differential equations (ODEs) after spatial discretization using the finite difference method, which can be numerically integrated using an ODE solver. We also extend the equidistant grid in both space and time used by Baffou et al.[41] to allow for variations in either dimension. In space we allow for multiple layers that have different spacing between discretized points in space. By using a smaller spacing in places where the gradients are high, such as near the nanoparticle in space and near the beginning of the simulation in time, a better balance can be achieved between accuracy and computation time.

Results and Discussion

Modeling

Using this model, we compare the bare 30 nm gold nanoparticles with core–shell nanoparticles with a gold core of the same diameter and a silica shell in water by focusing on the temperature at the various interfaces and the radial temperature profiles at several points in time (Figures 3a–d). A silica shell thickness of 2 nm was chosen as, while thin shells are in principle desirable for the fastest temperature rise, this is thick enough to be able to be synthesized without pinholes.[26,52] For these calculations, we use a fluence of 16 J m^{-2} to ensure the maximum temperature of the silica shell is at most 300 °C when heated from room temperature, as at this temperature thin silica shells are stable while degradation has been observed at higher temperatures in literature.[52] The material properties used in the calculations are given in Table 1 and the used values for the interfacial conductance G are given in Table 2. A more complete overview of values found are tabulated in Table S1. The variability in these values and their impact on the modelling results is discussed further in the text.

Table 2. Values of the interfacial conductance G used in the model. For interfaces marked with * no literature data was available, and that of similar interfaces was used as explained in section S2.2.

Interface	G (MW m^{-2} K^{-1})
Gold↔silica[47]	134
Gold↔water[48]	105 (15)
Gold↔air[49]	4 (4)
Gold↔ethanol[49]	32
Gold↔polyurethane*[49]	32
Silica↔water[50]	330
Silica↔air*[49]	4 (4)
Silica↔ethanol*[51]	87
Silica↔polyurethane*[51]	87

While the temperature profile of the core is similar for both nanoparticles in aqueous environment (Figures 3a and c, blue lines), the temperature profile of the water at the interface with the nanoparticle is pronouncedly different (same figures, red lines). In the presence of a shell, there is a delay before the occurrence of any significant temperature rise, and the temperature rises more slowly. This results in a maximum temperature increase that is both lower (from 93 °C to 68 °C) and reached later (from 72 ps to 105 ps). This can be interpreted as the silica acting as a thermal insulator, delaying the heat transfer from the core to the water which results in a slower temperature rise and the maximum temperature being reached later. The maximum temperature is lower for two reasons. First, while the heating is slower, the cooling capacity of the water is not affected. Secondly, because the water interface has a larger surface area over which the heat is dissipated for the core–shell nanoparticle.

Applications in gas atmosphere offer an environment where the material properties governing heat transport differ significantly from that in liquid environments. Therefore, the same bare and core–shell nanoparticle as for water were also modeled using air as the environment (Figures 3e–h). When compared to nanoparticles in water, the maximum temperature increases are clearly higher for both bare (compare Figures 3a and e) and core–shell (compare Figures 3c and g) nanoparticles, and the temperature decreases much more slowly afterwards in air (Figure S3). It also takes longer in air to reach the maximum temperature, in particular the duration of reaching the last 10%. Excluding the final 10% and focusing on the time the main temperature rise takes, to 90% of ΔT_{max} (Table 3), we see that for the bare nanoparticles this rise is much faster in air

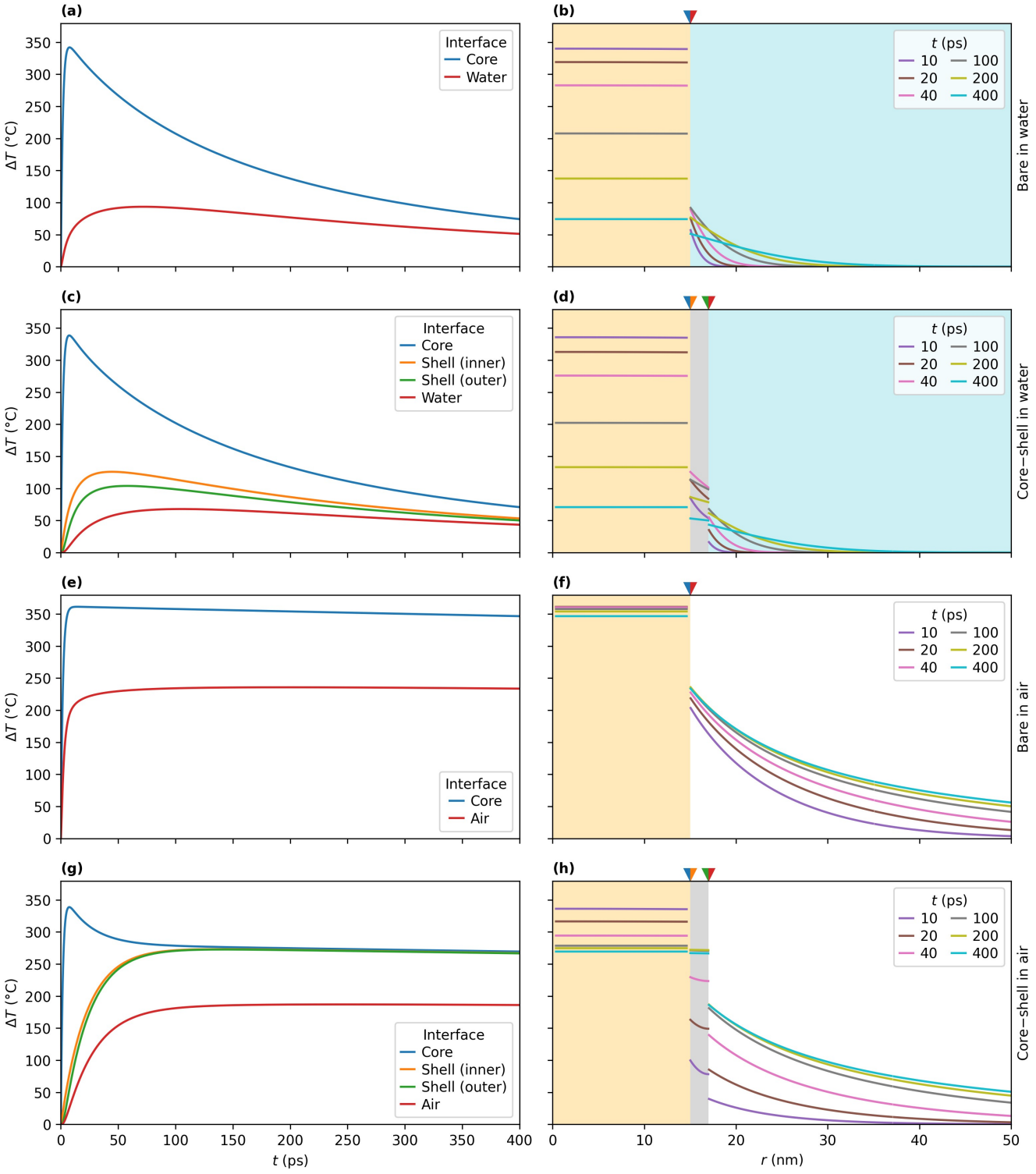

Figure 3. Modeled temperature profiles of bare and core–shell nanoparticles in water or air, with left the temporal profiles at the interfaces and right the radial profiles, and with the radial position of the temporal profiles indicated at the top. (a) Temporal and (b) radial temperature profile of a bare nanoparticle in water. (c) Temporal and (d) radial temperature profile of a core–shell nanoparticle in water. (e) Temporal and (f) radial temperature profile of a bare nanoparticle in air. (g) Temporal and (h) radial temperature profile of a core–shell nanoparticle in air.

compared to water (14 ps versus 30 ps), while the opposite is true for nanoparticles with a shell (66 ps versus 53 ps).

As water has relatively unique thermal properties, the modeling was repeated for other solvents, as well as a polyurethane system similar to the PUU used as the experimental

Table 3. Maximum temperature increases (ΔT_{max}) and the time in which 90% of this is reached ($\Delta t_{0.9max}$) for a fluence of 16 J m^{-2}.

Environment	Shell	ΔT_{max} (°C)	$\Delta t_{0.9max}$ (ps)
Water	No	93	30
	Yes	68	53
Air	No	236	14
	Yes	187	66
Ethanol	No	121	79
	Yes	114	78
Polyurethane	No	104	87
	Yes	99	81

system, although less literature on accurate values of *G* exists for these materials. For organic solvents, we focus here on ethanol (Table 3) which shows similar results as other organic solvents (Table S2) but for which the most literature on *G* was available.[49,51] In its temperature profiles (Figure S2) ethanol shows a maximum temperature intermediate to that in both water and air, but a slower main temperature rise than these media. These temperature profiles also show that for ethanol the cooling rate of the core is intermediate to that of water and air (Figure S3). Interestingly, the main temperature rise of ethanol is practically identical with and without a silica shell. For the polyurethane system, no data on *G* was found in literature, and values for ethanol were used (Table 3). Given that other, more hydrophobic, organic solvents have similar values (Table S2), this is a reasonable approximation that can be used to highlight the differences in material properties between ethanol and polyurethane. The maximum temperature for polyurethane is intermediate to water and ethanol, but the main temperature rise is slower than in these media.

The radial profile for the bare nanoparticle in water (Figure 3b) shows that the high temperatures in the water are initially confined to a thin layer around the nanoparticle, where in the couple of nanometers closest to the nanoparticle much higher temperatures are reached than further away from the nanoparticle. Over time, the excess heat dissipates over a greater volume. It is known that femtosecond illumination leads to more confined heating than continuous-wave illumination.[41] Considering all radial profiles (Figures 3b, d, f and h and Figures S2b and d), we can see that there is a large difference between those in water and those in air: a much larger volume of the environment is heated for the latter. For ethanol a smaller volume of the environment is heated in comparison to water, but the difference is less stark than between water and air. When comparing bare and core–shell nanoparticles with the same surrounding environment, the spatial temperature distribution of the environment is similar for bare and core–shell nanoparticles for all three media, with the main differences being due to the slower heating of the environment when a shell is present.

The interfacial conductance *G* is an important factor in the temperature profile of both bare and core–shell nanoparticles. The values used for the calculations are shown in Table 2, with a more complete overview of values in literature in Table S1. Since the values for the various interfaces of nanoparticles suspended in water are the most studied, we focus on the nanoparticles with water as their environment for this discussion. For the gold–water interface in bare gold nanoparticles, the value of *G* is more than twice as high with a hydrophilic surface functionalization compared to hydrophobic one.[51] For gold nanorods, the interfacial conductance can vary from 45 MW m^{-2} K^{-1} to 450 MW m^{-2} K^{-1},[53,54] and simulations using *G* values in this range show a large variation in resulting temperature profiles (Figure S4): both the heating rate and maximum temperature of the water are greatly increased with higher values of *G*, while in turn the nanoparticle itself cools more rapidly. Comparisons with literature and experimental results should therefore focus on trends rather than precise values, unless care has been taken to match the interfacial conductance, *e.g.* through fitting to theoretical models.[53–55]

The interfaces present in core–shell nanoparticles in water, gold–silica and silica–water, are less studied than the gold–water interface. Because these values are obtained by molecular dynamics or experimentally for layered systems instead of nanoparticles, the applicability to synthesized core–shell nanoparticles should therefore be determined experimentally. As for the gold–water interface, literature values for the gold–silica and especially the silica–water interface vary greatly, from 39 MW m^{-2} K^{-1} to 222 MW m^{-2} K^{-1} and from 220 MW m^{-2} K^{-1} to 2380 MW m^{-2} K^{-1}, respectively.[50,56–58] Applying different combinations of these values in the model yields pronouncedly different temperature profiles (Figure S5). The temporal temperature profile of the core is determined for an important part by the interfacial conductance of the gold–silica interface, both because this interface is in direct contact with the core and because its values are relatively low, making it the limiting factor in heat dissipation in an aqueous environment. On the other hand, the temperature profile of the water at the interface with the silica shell is influenced greatly by both interfacial conductances, and a higher value of either one means the maximum water temperature is higher and is reached earlier in time.

Various of the observed differences between model systems discussed can be explained by differences in the material or interface properties, as given in Tables 1 and 2. For example, the radial temperature profile in the medium is mostly determined by the thermal diffusivity of that medium: since that of air is two orders of magnitude larger than that of water, a much larger volume is heated significantly (Figures 3b and f). That the reached temperatures in air are still much higher than in water, is because much less heat is extracted from the nanoparticle to reach these high temperatures in the environment, due to the volumetric heat capacity of air being three orders of magnitude smaller than that of water. Other properties also influence the maximum temperature, such as the interfacial conductance, but these do not explain the differences between materials. These trends also extend to ethanol (Figure S2) and polyurethane, which have intermediate volu-

metric heat capacities and lower thermal diffusivities compared to air and water.

Experimentally, time-resolved techniques can be used to study the temperature profiles of both plasmonic nanoparticles themselves as well as their environment. The former is more common, as this can readily be measured using transient absorption spectroscopy in the visible domain. In comparisons between gold nanoparticles with and without a silica shell, the core temperature decay was faster when a shell was present.[59] For other inert shells, such as polyelectrolyte multilayer coatings, the core temperature decay is faster for bare nanoparticles.[55] In our work, the core temperature without shell (Figure 3a, blue line) decays slightly more slowly compared to when a shell is present (Figure 3c, blue line), but the difference is minimal and less than reported previously.[59] This can be because the experimental silica shells are porous, or because the interfacial conductances between gold and silica in our model are smaller than for the these reported core–shell nanoparticles. Figures S4 and S5 show that there are values of *G* that explain a faster decay when a shell is present.

Using MIR-TA spectroscopy, the solvent around the nanoparticles can be probed to measure the temperature of the surroundings. Literature experiments using this technique show that for gold nanorods in water, porous silica shells slow down the heat transfer to the environment.[33] Our simulations also show much slower heating of water when a shell is present (Figure 3c, red line) compared to a bare nanoparticle (Figure 3a, red line). A slower heating of the surroundings while the core cools down more rapidly is possible because the silica shell acts as a heat sink that is heated by the core before it can in turn heat its surroundings.

Experimental

While the modeling in the previous section shows a main temperature rise is possible in tens of picoseconds, we also want to probe how quickly high temperatures can be reached in the nanoparticle surroundings experimentally. In order to do this, we study a thermally activated process in this work, where the spectrum changes above a certain temperature, and use MIR-TA to measure the time dynamics of these spectral changes. For this purpose, we employ a PUU, namely PHTD (Scheme 1a), as these can show temperature-dependent changes in their hydrogen bonding network.[60,61]

Variable-Temperature Fourier-Transform Infrared Spectroscopy

Experimentally, the temperature-dependent spectral changes associated with changes in the hydrogen bonding network of PHTD were first assessed using transmission variable-temperature Fourier-transform infrared (VT-FTIR) during multiple heating cycles. Here, we focus on a single heating cycle and the C=O stretch vibrations (see section S3.2 for other cycles and other vibrations). The C=O stretch vibrations are present from around 1750 cm^{-1} to 1600 cm^{-1} (Figure 4a) and can be divided into the urethane C=O stretch vibrations around 1700 cm^{-1} and the urea C=O stretch vibrations around 1630 cm^{-1}.[62,63] Of these, the former shows a clear blueshift when heated. This can be seen as a decrease in hydrogen-bonded urethane C=O stretch signal at 1690 cm^{-1} and an increase in free urethane C=O stretch intensity at 1720 cm^{-1}, with an isosbestic point at 1703 cm^{-1}.[62–64] Most of this spectral change is abrupt, happening from 70 °C to 90 °C, which can be most clearly seen from the absorbance against temperature at the edges of these peaks, where the change in absorbance is maximal (Figure 4b). In particular, the decrease at 1680 cm^{-1} is abrupt, which can also be seen in the calculated difference spectra (Figure 4c). The abrupt change occurs simultaneously with the decrease of hydrogen-bonded N–H stretch vibrations and increase of the corresponding free vibrations (Figure S12), further indicating that the spectral changes are indeed due to a partial breakdown of the C=O···H–N hydrogen bonding network of those moieties (Scheme 1b). Such a sudden shift in absorbance has also been observed for other PUUs,[60,61] for example at the

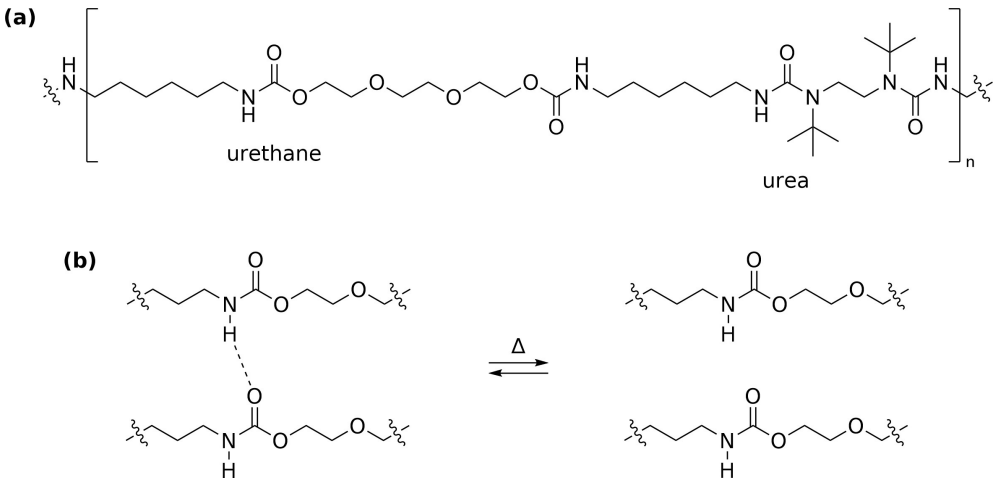

Scheme 1. Structure of poly[(hexamethylene diisocyanate)-*alt*-(triethylene glycol; *N*,*N*′-di-*tert*-butylethylenediamine)] (PHTD): (a) structure of the polymer, indicating the urethane and urea moieties containing C=O bonds and (b) breaking of hydrogen bonds of urethane at higher temperatures.

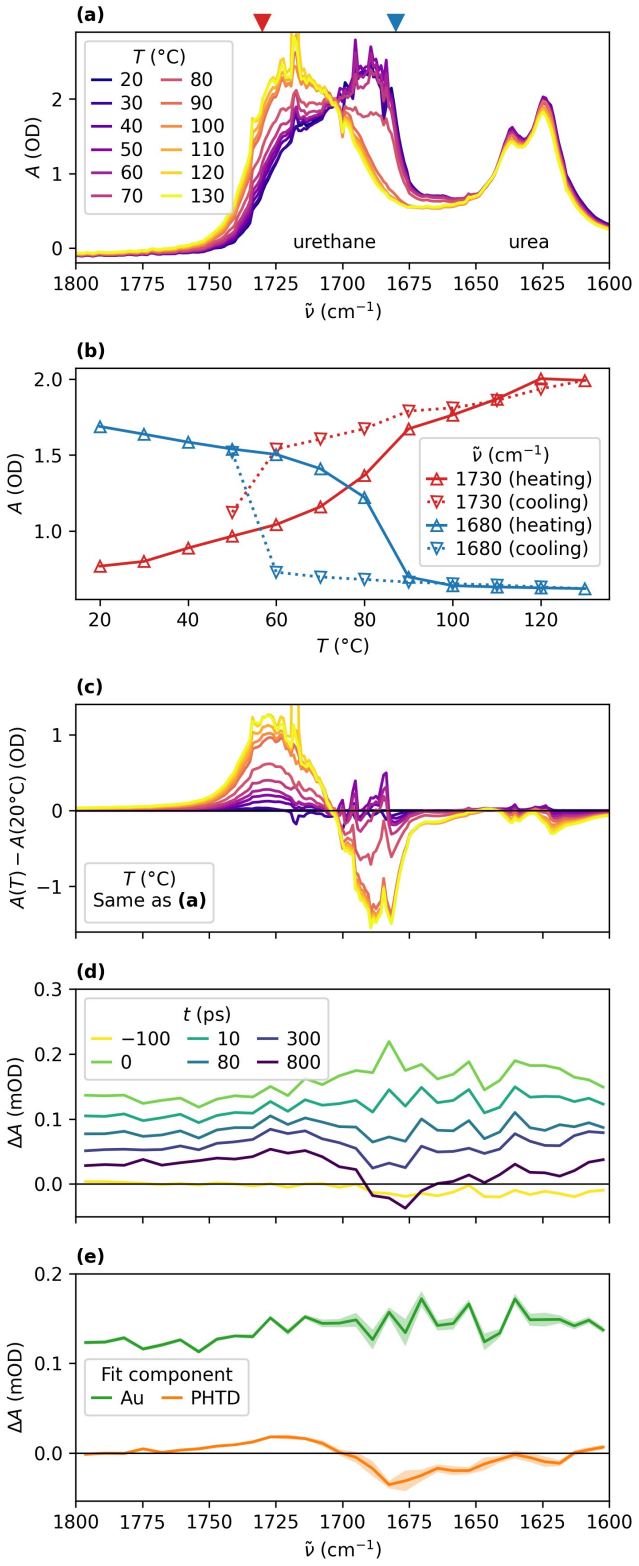

Figure 4. Infrared results of PHTD around the C=O stretch vibration. (a) The VT-FTIR spectra while heating from 20 °C to 130 °C. (b) The VT-FTIR absorption as a function of temperature for 1730 cm^{-1} and 1680 cm^{-1} while heating from 20 °C to 130 °C and subsequently cooling to 50 °C. (c) The difference spectra during heating between elevated temperatures and room temperature calculated from (a). (d) Measured MIR-TA difference spectra at various time points and (e) spectral components of the fit of Eq. (6) to these spectra, with shaded areas indicating estimated error.

melting temperature,[61] but not all polymers in this class show this behavior.[62] During cooling, the changes in absorbance appear to be fully reversible, but the reversal occurs at the lower temperature of 50 °C (Figures 4b and S12). This observed hysteresis was not expected as it is generally occurs when stronger hydrogen bonding motifs are present.[65]

Due to the bulky *tert*-butyl group on the urea, this urea contains a dynamic covalent bond that can be broken at elevated temperatures.[66] This was observed at higher temperatures than the change in hydrogen bonding network, and only in low amounts (Figures S9 and S12). As a result, the effect on absorption in the C=O stretch region of this was negligible.

Mid-Infrared Transient Absorption Spectroscopy

For MIR-TA experiments, a film of PHTD containing gold–silica core–shell nanoparticles was studied with a pump at 400 nm and a probe in the mid-infrared around the C=O stretch region. Based on the VT-FTIR spectra in this region (Figure 4a), the expected difference spectrum due to heating can be calculated for different temperatures (Figure 4c). At lower temperatures, this shows a weak positive signal above 1703 cm^{-1}. From 90 °C and above, this shows a strong positive signal above and a strong negative signal below the isosbestic point at 1703 cm^{-1} for the urethane C=O stretch, as well as weak negative signals at 1630 cm^{-1} and 1520 cm^{-1} for the urea C=O stretch. This can be combined with modeling the heat transfer of the nanoparticle in a polymer matrix using the previously presented methodology to determine the expected time profile in the MIR-TA data (Figure 5). The temporal profile (Figure 5a) shows a fast temperature rise, and the radial profile (Figure 5b) shows high temperatures are only reached close to the nanoparticle itself. The latter suggests any collective heating effects would be minimal, which was confirmed to be the case for the used experimental conditions (see section S3.3).[67] Since the absorbance of the polymer changes significantly at 90 °C, the temporal profile of the volume of the polymer reaching a temperature of at least 90 °C was determined for various fluences (Figure 5c), as this is expected to determine the magnitude of the measured transient signals for a major part. This shows a short delay in the order of tens of ps before any polymer reaches this temperature, followed by a rapid rise in volume of this temperature. On the order of 100 to 100 s of ps, the maximum volume is reached, after which the volume declines on the same time scale.

In the MIR-TA spectra (Figure 4d), a spectrally uniform induced absorption is visible at short time delays. Over time, this signal decays, and additional spectral features appear: an induced absorption at 1750 cm^{-1} to 1700 cm^{-1} and a bleaching at 1700 cm^{-1} to 1650 cm^{-1}. These features start to appear between 40 ps and 100 ps and are most pronounced towards longer delay times, especially in the spectrum at 800 ps. We assign the initial wavelength-independent induced absorption to the gold nanoparticles themselves, since the increased electron temperature after excitation can lead to induced absorption via processes like Fermi smearing.[68,69] While the

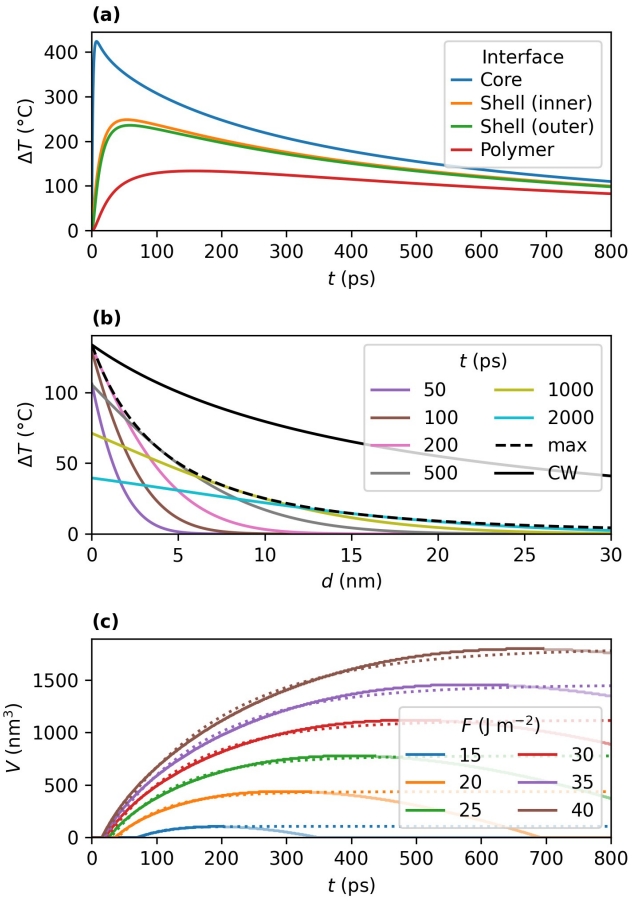

Figure 5. Modeling results of a plasmonic gold–silica core–shell nanoparticle with a diameter of 30 nm and a shell thickness of 1.5 nm in a polyurethane matrix after femtosecond illumination at 20 J m^{-2}. (a) Temporal temperature profile at the interfaces. (b) Radial temperature profile at different times at distance d from the nanoparticle over time. The maximum temperature and temperature under continuous wave illumination (scaled to the same temperature at the nanoparticle surface) are also shown. (c) Volume of the polymer above 90 °C for different fluences over time. Dotted lines indicate fits of Eq. (5) to the volume rise.

electron temperature is most increased immediately following excitation, it remains higher than room temperature during the experiment, as it follows the cooling of the nanoparticle once the electron and lattice temperature are in equilibrium after the first picoseconds. The spectral features at longer delay times are in agreement with the expected difference spectrum from PHTD upon heating based on VT-FTIR experiments (Figure 4c).

In order to analyze these signals more quantitatively, fitting of the spectrum can be used. Since the absorbance is dependent on local temperature rather than photoexcited charge transfer, standard kinetic models used in pump–probe spectroscopy do not necessarily apply. For the signal from the gold nanoparticles over time, it has been shown in literature that the heat dissipation can be empirically approximated using a stretched exponential:[70]

$$\Delta A_{\mathrm{Au}}(t) \propto \mathrm{e}^{-\left(\frac{t}{\tau_{\mathrm{Au}}}\right)^{\beta_{\mathrm{Au}}}} \tag{4}$$

with two temporal parameters: a time constant τ_{Au} and a stretching parameter β_{Au}. In some studies a double exponential is used instead,[59] but the stretched exponential uses a smaller number of parameters and fits simulated electron temperature better for plasmonic nanoparticles.[32]

The signal of PHTD is a combination of heat diffusion from the nanoparticle to the polymer and thermal switching behavior of the polymer. Fitting this therefore requires different methods than those used for thermalization in molecular systems.[71] We propose, based both on theoretical considerations and numerical simulation as described below, one minus a delayed exponential:

$$\Delta A_{\mathrm{PHTD}}(t) \propto 1 - \mathrm{e}^{-\frac{\max(0,\, t-\theta_{\mathrm{PHTD}})}{\tau_{\mathrm{PHTD}}}} \tag{5}$$

again using two temporal parameters: a time constant τ_{PHTD} and a time offset θ_{PHTD}. This time offset represents the delay before the surroundings are heated above the temperature where the absorption spectrum changes, and the time constant how quickly the volume of the polymer where this temperature is reached increases. The choice for this function is motivated by using a limited number of parameters, and describing the switching behavior of the polymer observed qualitatively. The heat transfer modeling of a nanoparticle with polymer surroundings, as described above, shows that this function reasonably approximates the increase in volume that reaches a certain temperature (Figure 5c). The decrease of the volume above this temperature at longer times due to heat dissipation is not incorporated because no transient signal decrease is observed experimentally on the given timescale and also not expected to due to the hysteresis displayed by the polymer (Figures 4b and S12).

Eqs. (4) and (5) can be combined to show the MIR-TA signal can be modeled as:

$$\Delta A(\tilde{\nu}, t) = \alpha_{\mathrm{Au}}(\tilde{\nu})\mathrm{e}^{-\left(\frac{t}{\tau_{\mathrm{Au}}}\right)^{\beta_{\mathrm{Au}}}} + \alpha_{\mathrm{PHTD}}(\tilde{\nu})\left(1 - \mathrm{e}^{-\frac{\max(0,\, t-\theta_{\mathrm{PHTD}})}{\tau_{\mathrm{PHTD}}}}\right) \tag{6}$$

with, in addition to the four parameters describing the temporal dependence, two spectra $\alpha(\tilde{\nu})$ to describe the spectral dependence.

Using a constrained fit (see section S3.4), the temporal parameters (Table 4) and two spectra (Figure 4e) can be fit. When considering the spectra, α_{Au} describing the stretched exponential is spectrally uniform as expected, while the expected difference spectrum from the VT-FTIR experiments

Table 4. Fit parameters and coefficient of determination for Eq. (6).

Parameter	Fit value
τ_{Au} (ps)	499 (21)
β_{Au}	0.54 (2)
τ_{PHTD} (ps)	45 (13)
θ_{PHTD} (ps)	60 (9)
r^2	0.876

(Figure 4c) is visible in α_{PHTD} of the delayed exponential. The time traces of this fit (Figures 6a–c) show both the fit of only the stretched exponential fit component (dotted lines) and the complete fit of Eq. (6) (continuous lines), showing how the fit component of the delayed exponential explains part of the observed data at the positive and negative peaks of α_{PHTD}. To examine the contribution of the latter more closely, only that fit component is plotted in Figure 6d by subtracting the contribution from the stretched exponential. This shows the delayed heating is visible in the data at 1720 cm^{-1}, but the data quality at 1676 cm^{-1} is too poor to distinguish between heating starting only from after a delay or directly after excitation. A perfect fit would in any case not be expected, since Eq. (5) assumes highly monodisperse nanoparticles and that PHTD shows only a change in absorbance at a single temperature, which are both only correct by approximation. The kinetics of the hydrogen bond breaking are also assumed to be negligible in comparison to the heating process, and the observed fitting shows that the dynamics of hydrogen bond breaking is at least not significantly slower than the heating rate. This may indicate that the breaking of hydrogen bonds is not accompanied by significant conformational changes of the polymer, such as rotation of molecular units around the polymer backbone, as these are expected to be slower. Rather, such conformational changes may occur only after the hydrogen bond breaking, or they may be very limited. In total, the determined time dynamics of the hydrogen bond breaking of PHTD shows that a femtosecond light pulse can induce a thermal process in the surroundings of a gold–silica core–shell nanoparticle on the time scale predicted here numerically.

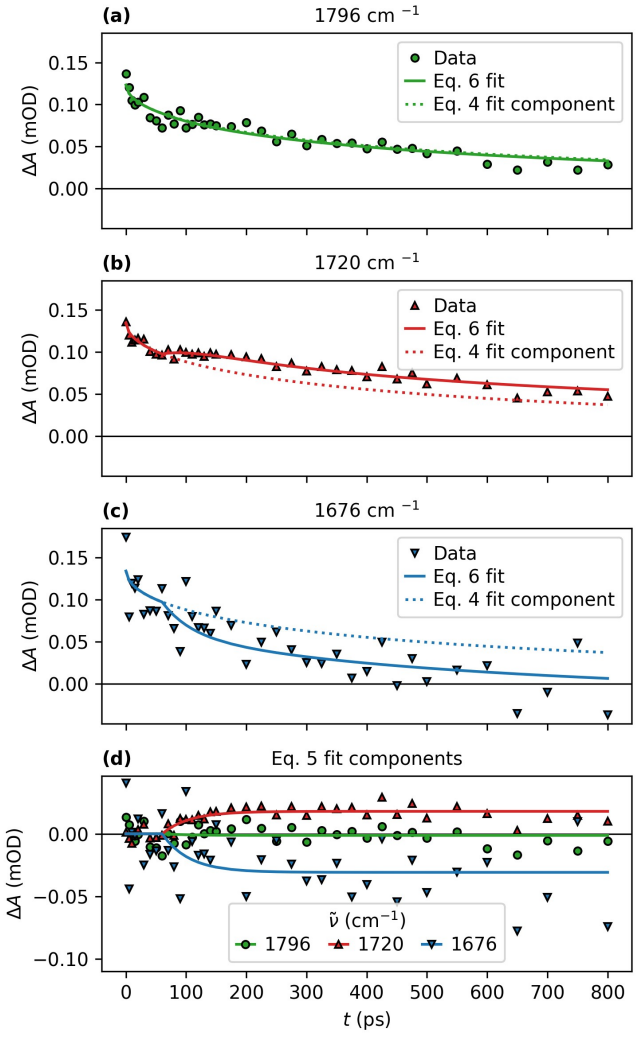

Figure 6. Time traces of MIR-TA data of PHTD at different wavenumbers around the C=O stretch vibration, including fits to Eq. (6). (a) Data and fit at 1796 cm^{-1}, with no PHTD contribution. (b) Data and fit at 1720 cm^{-1}, with a positive PHTD contribution. (c) Data and fit at 1676 cm^{-1}, with a negative PHTD contribution. (d) The same fits, but only the component of Eq. (5) to highlight the differences due to heating.

While the cooling of plasmonic nanoparticles after femtosecond illumination is often studied in literature,[32,55,59,72–74] few studies focus on directly probing the heating of the environment. The immediate environment can be probed by Raman spectroscopy of adsorbates directly on gold nanoparticles, which shows heating and cooling within picoseconds.[75] This is likely due to direct energy transfer from the photoexcited plasmon to the vibrational levels of these adsorbates.[75] Using MIR-TA spectroscopy, the environment can be probed collectively, for example using a temperature-dependent vibrational mode of water.[33] In comparison to our work, this study observes a heating signal without delay, and slower heat transfer,[33] which can both be attributed to the studied processes being linearly dependent on temperature, without switching behavior. Thermal switching behavior induced by plasmonic nanoparticles has been researched in polymers where such a delay is observed, but on a hydrogel where water is ejected during the phase transition, which is therefore a slower processes happening after tens of nanoseconds,[76] while we show a process with a much shorter delay.

Conclusions

Previous work on numerically integrating the heat equation to calculate temperature profiles for bare gold nanoparticles was extended to core–shell nanoparticles, and a wider range of surrounding media, to determine their potential as ultrafast nanoheaters. In all cases, the main temperature rise occurred within the order of tens of picoseconds, also when a 2 nm thick silica shell was present, showing that such a shell does not majorly impair the heating potential of a plasmonic nanoparticle. For both water and air, the heating of the environment is delayed, slower, and reaches a lower maximum temperature increase when a shell is present compared to a bare nanoparticle. Yet, in some cases where the interfacial heat conductance between gold and the surrounding medium is significantly lower than that between silica and the surrounding medium, a silica shell may actually accelerate the heating of the surrounding medium. When comparing water with air as surrounding medium, the latter shows a higher maximum temperature increase for the same fluence, for both bare and core–shell nanoparticles, due to the lower volumetric heat capacity of air. As a result of the lower thermal diffusivity of

water, the heating effect of water in particular is largely confined to several nanometers from the surface of the nanoparticle, while surrounding air will be heated over a much larger volume. Organic materials such as solvents and polymers show temporal and spatial temperature profiles roughly in between that of air and water, but closer to the latter.

To experimentally validate whether these time scales can also be achieved in practice, gold–silica core–shell nanoparticles embedded in a matrix of the polymer PHTD were used for MIR-TA spectroscopy. This poly(urethane-urea) was shown to undergo significant changes in its hydrogen bonding network at 90 °C, which is reflected in changes in its infrared spectrum. Using MIR-TA spectroscopy, the polymer with nanoparticles embedded showed a clear heating signal of the polymer on top of the cooling signal from the gold nanoparticles in the C=O stretch region. This signal seems to exhibit a delayed appearance, unlike literature studies on linear processes, which followed the expected time dynamics of the temperature increase. These results demonstrate that a femtosecond light pulse can be used to quickly initiate a thermal process in the surroundings of a plasmonic nanoparticle. Interestingly, this also shows experimentally that the kinetics of the hydrogen bond breaking are faster than the heating kinetics (which takes tens of picoseconds). This may indicate that the breaking of hydrogen bonds doesn't occur concerted with significant conformational changes of the polymer, such as rotation of molecular units around its backbone, as these are expected to be slower.

A temperature rise occurring in the order of tens of picoseconds shows the potential to use gold–silica core–shell nanoparticles to study other thermally initiated processes, *e.g.* to elucidate short-lived reaction intermediates with lifetimes in the nanosecond regime, or down to higher end of the picosecond regime. In contrast to previously reported methods to optically induce ultrafast temperature, these can be used in a wide range of media (as opposed to terahertz, far- or near-infrared light for heating aqueous media), and are chemically inert (as opposed to heating via organic dyes). This article shows what kind of temporal and spatial temperature profiles can be expected when using gold–silica core–shell nanoparticles in femtosecond-pulsed pump–probe spectroscopy in different media.

Experimental Section

Modeling

The heat transfer model as described in section S1 was run with certain parameters on different nanoparticle geometries as described hereafter. A gold nanoparticle with a diameter of 30 nm in water was used as a basis for the studied systems. To look at the effect of the presence of a silica shell, we consider this particle with and without a 2 nm silica shell around it. Additionally, this was repeated with air, ethanol, or polyurethane as the environment instead of water.

The heat generated in the nanoparticle is entirely dependent on the energy absorbed, which is determined by the absorption cross section and the fluence. The absorption cross section of the nanoparticle is dependent on the refractive index of its surroundings and therefore changes based on the surrounding solvent or gas, as well as a potential silica shell. In order to compare the effect of different geometries on the heat transfer and not the effect on the absorption cross section at a certain wavelength, a constant absorption cross section of 797 nm^2 – that of a bare 30 nm gold nanoparticle in water at 400 nm – was used for all calculations. A single fluence of 16 $J m^{-2}$ at 400 nm was used, as obtained temperature profiles can be scaled to other fluences using Eq. (S24).

For comparison with the experimental system, the model was also used on a gold–silica core–shell nanoparticle with a core diameter of 30 nm and a shell thickness of 1.5 nm embedded in a polyurethane matrix. Heat transfer with the described nanoparticle was modeled under both femtosecond and continuous wave illumination at 400 nm. The linearity between modeled temperature and input fluence or irradiance was used to determine temperature profiles for different fluences/irradiances using Eq. (S24).

Synthesis

Chemicals and solvents were commercially acquired from Merck, TCI and Alfa Aesar and used without further purification.

Poly[(Hexamethylene Diisocyanate)-alt-*(Triethylene Glycol;* N,N′-*di*-tert-*Butylethylenediamine)]*

673 mg (4.0 mmol) of hexamethylene diisocyanate was dissolved in 4 mL anhydrous DMSO. Under argon and stirring, 230 mg (1.33 mmol) *N,N′*-di-*tert*-butylethylenediamine was added to the solution while cooling in an ice bath. The ice bath was removed and 350 mg (2.66 mmol) anhydrous triethylene glycol was added to the solution. The flask was sealed under argon and stirred at 60 °C overnight. The obtained solution of PHTD in DMSO was used as such in subsequent experiments.

Gold–Silica Core–Shell Nanoparticles

This method was adapted from a literature procedure.[77] All solutions are in Milli-Q water unless otherwise specified.

0.5 mL of 0.2 M cetyltrimethylammonium bromide at 30 °C was mixed with 0.5 mL of 0.5 mM chloroauric acid. To this, 10 μL of a freshly prepared solution of 13.8 mg (365 μmol) sodium borohydride in 594 μL Milli-Q water was added. The resulting "seed solution" was aged for 30 min before use in the next step. Meanwhile, 5.410 g (14.8 mmol) of cetyltrimethylammonium bromide and 0.760 g (2.50 mmol) of sodium oleate were dissolved in 150 mL of Milli-Q water under stirring at 35 °C. Once fully dissolved, 1.8 mL of 32 mM silver nitrate was added, and subsequently 150 mL of 1 mM chloroauric acid was added. The solution was stirred for 1 h until it was colorless, and 0.9 mL of concentrated 37 % hydrochloric acid was added. Under vigorous stirring, 100 μL of a solution of 18.9 mg (107 μmol) L-ascorbic acid in 224 μL Milli-Q water was added, followed by 60 μL of the "seed solution" synthesized in the last paragraph. Once fully mixed, stirring was stopped and the solution was aged overnight.

The aged solution was diluted by adding 300 mL of Milli-Q water. Under vigorous stirring, 343 μL of a solution of 21.5 mg (97 μmol) (3-aminopropyl)triethoxysilane in 4.158 g Milli-Q water was added. After 20 min, the following solution was added: 1.28 mL of 27 % sodium silicate mixed with 60 mL of Milli-Q water and acidified to pH 10.3 with a 0.1 M sulfuric acid solution. The pH of this solution

was adjusted to 10.3 with a 0.5 M sodium hydroxide solution. After 15 min, the solution was placed in a pre-heated 90 °C oil bath for 1.5 h. The solution was centrifuged for 30 min at 6 krpm, decanted, and the pellet was resuspended in 50 ml Milli-Q water. The centrifugation step was repeated with resuspension in Milli-Q water, which was used for characterization. For use in ir applications together with PHTD, the centrifugation step was repeated followed by resuspension in 5 ml DMSO.

The aqueous nanoparticle solution was characterized using a uvvis spectrophotometer (PerkinElmer Lambda 40). For TEM characterization, a drop of aqueous nanoparticle solution was cast on a carbon film on copper mesh TEM grid, dried, and analyzed on a TEM (Jeol JEM-1400Plus). Obtained micrographs were analyzed using ImageJ,[78] through its *Analyze Particles* and *Measure* functionalities, to measure core size/shape and shell thickness, respectively.

Variable-Temperature Fourier-Transform Infrared Spectroscopy

A CaF_2 window (Crystran; 25 mm diameter, 2 mm thick) was hydrophilized using plasma cleaning. Two drops of the PHTD solution in DMSO as prepared above were cast on the hydrophilized CaF_2 window. The window was then dried, first under nitrogen flow and then under vacuum.

The sample was analyzed by VT-FTIR spectroscopy on an FTIR spectrometer (Thermo Scientific Nicolet 8700) equipped with a temperature-controlled demountable liquid cell (Harrick) in transmission. Atmospheric correction was performed on measured spectra to minimize water vapor peaks.

Mid-infrared Transient Absorption Spectroscopy

A CaF_2 window (Crystran; 25 mm diameter, 2 mm thick) was hydrophilized using plasma cleaning. A 2:1 mixture (v/v) of PHTD and nanoparticle solutions, both in DMSO as prepared above, was made and two drops of this solution were cast on the hydrophilized CaF_2 window. The window was then dried, first under nitrogen flow and then under vacuum.

A Ti:sapphire regenerative amplified laser (Spectra-Physics Spitfire Ace) provided pulses at 800 nm with a duration of 35 fs and a repetition rate of 1 kHz. A fraction of this beam was used to pump a OPA (Spectra-Physics TOPAS Prime) to generate signal and idler beams, that were recombined in a NDFG stage based on a GaSe crystal to generate tunable IR pulses with a duration of ~100 fs. This IR beam was divided using a wedged CaF_2 window into a reference and a probe beam using the front and back reflections, respectively. Another fraction of the 800 nm beam was modulated using a mechanical chopper at 500 Hz and frequency-doubled in a BBO crystal to yield pump pulses of 400 nm. These pump pulses were delayed using a translational stage, which allowed for delays up to 1.4 ns. The probe beam was focused on the sample using an off-axis parabolic mirror, and the pump beam was partially focused using a lens and spatially overlapped with the probe beam. The probe beam was re-collimated and subsequently focused, together with the reference beam, on the entrance slit of the spectrograph (Horiba Scientific Triax 180), which focuses the spectrally dispersed image of both beams on a 2×32 pixel MCT detector (Infrared Associates).

Fitting of measured spectra was performed using SciPy[79] using the method of least squares, and obtained covariance matrices were used to determine both parameter and prediction uncertainty.[80]

Supporting Information

The authors have cited additional references within the Supporting Information.[81–88]

Acknowledgements

This publication is part of the project "Nanoheaters unravel catalytic reactions with ultimate time resolution" with project number VI.Vidi.193.151 of the research programme Vidi ENW which is (partly) financed by the Dutch Research Council (NWO).

Conflict of Interests

The authors declare no conflict of interest.

Data Availability Statement

The data that support the findings of this study are openly available in 4TU.ResearchData at https://doi.org/10.4121/3d09872e-c111-4476-b339-30cc1f6557e8.[89]

Keywords: femtochemistry · laser spectroscopy · nanoparticles · surface plasmon resonance · time-resolved spectroscopy

[1] A. H. Zewail, *J. Phys. Chem. A* **2000**, *104*, 5660.
[2] C. Wang, A. Malinoski, *J. Chem. Phys.* **2022**, *157*, 160901.
[3] T. Elsaesser, *Chem. Rev.* **2017**, *117*, 10621.
[4] R. Mincigrucci, M. Kowalewski, J. R. Rouxel, F. Bencivenga, S. Mukamel, C. Masciovecchio, *Sci. Rep.* **2018**, *8*, 15466.
[5] A. Bhattacherjee, M. Sneha, L. Lewis-Borrell, O. Tau, I. P. Clark, A. J. Orr-Ewing, *Nat. Commun.* **2019**, *10*, 5152.
[6] A. S. Marshall, R. A. Rogers, J. W. Perry, W. J. Brittain, *J. Phys. Org. Chem.* **2016**, *29*, 221.
[7] M. Maiuri, M. Garavelli, G. Cerullo, *J. Am. Chem. Soc.* **2020**, *142*, 3.
[8] J. Zhu, X. Wu, D. M. Lattery, W. Zheng, X. Wang, *Nanoscale Microscale Thermophys. Eng.* **2017**, *21*, 177.
[9] G. B. Park, T. N. Kitsopoulos, D. Borodin, K. Golibrzuch, J. Neugebohren, D. J. Auerbach, C. T. Campbell, A. M. Wodtke, *Nat. Chem. Rev.* **2019**, *3*, 723.
[10] A. Davó-Quiñonero, A. Bueno-López, D. Lozano-Castelló, A. J. McCue, J. A. Anderson, *ChemCatChem* **2016**, *8*, 1905.
[11] O. Müller, D. Lützenkirchen-Hecht, R. Frahm, *Rev. Sci. Instrum.* **2015**, *86*, 093905.
[12] M. K. Ko, H. Frei, *J. Phys. Chem. B* **2004**, *108*, 1805.
[13] Z. Wei, Y. Li, R. G. Cooks, X. Yan, *Annu. Rev. Phys. Chem.* **2020**, *71*, 31.
[14] R. H. Perry, T. J. Cahill, J. L. Roizen, J. Du Bois, R. N. Zare, *Proc. Nat. Acad. Sci.* **2012**, *109*, 18295.
[15] D. N. Mortensen, E. R. Williams, *J. Am. Chem. Soc.* **2016**, *138*, 3453.
[16] N. Wainstein, G. Ankonina, T. Swoboda, M. M. Rojo, S. Kvatinsky, E. Yalon, *IEEE Trans. Electron Devices* **2021**, *68*, 1298.
[17] F. Thibault-Starzyk, E. Seguin, S. Thomas, M. Daturi, H. Arnolds, D. A. King, *Science* **2009**, *324*, 1048.
[18] P. K. Mishra, O. Vendrell, R. Santra, *J. Phys. Chem. B* **2015**, *119*, 8080.
[19] P. K. Mishra, V. Bettaque, O. Vendrell, R. Santra, R. Welsch, *J. Phys. Chem. A* **2018**, *122*, 5211.
[20] B. Ashwood, N. H. C. Lewis, P. J. Sanstead, A. Tokmakoff, *J. Phys. Chem. B* **2020**, *124*, 8665.
[21] H. Ma, C. Wan, A. H. Zewail, *J. Am. Chem. Soc.* **2006**, *128*, 6338.
[22] H. Ma, C. Wan, A. H. Zewail, *Proc. Nat. Acad. Sci.* **2008**, *105*, 12754.

[23] C. M. Phillips, Y. Mizutani, R. M. Hochstrasser, *Proc. Nat. Acad. Sci.* **1995**, *92*, 7292.
[24] S. Chen, I. Y. S. Lee, W. A. Tolbert, X. Wen, D. D. Dlott, *J. Phys. Chem.* **1992**, *96*, 7178.
[25] V. Amendola, R. Pilot, M. Frasconi, O. M. Maragò, M. A. Iatì, *J. Phys. Condens. Matter* **2017**, *29*, 203002.
[26] J. F. Li, Y. F. Huang, Y. Ding, Z. L. Yang, S. B. Li, X. S. Zhou, F. R. Fan, W. Zhang, Z. Y. Zhou, D. Y. Wu, B. Ren, Z. L. Wang, Z. Q. Tian, *Nature* **2010**, *464*, 392.
[27] G. Baffou, F. Cichos, R. Quidant, *Nat. Mater.* **2020**, *19*, 946.
[28] A. Baldi, S. H. C. Askes, *ACS Catal.* **2023**, *13*, 3419.
[29] S. Moon, Q. Zhang, Z. Xu, D. Huang, S. Kim, J. Schiffbauer, E. Lee, T. Luo, *J. Phys. Chem. C* **2021**, *125*, 25357.
[30] K. Metwally, S. Mensah, G. Baffou, *J. Phys. Chem. C* **2015**, *119*, 28586.
[31] O. Ekici, R. K. Harrison, N. J. Durr, D. S. Eversole, M. Lee, A. Ben-Yakar, *J. Phys. D* **2008**, *41*, 185501.
[32] D. B. O'Neill, S. K. Frehan, K. Zhu, E. Zoethout, G. Mul, E. C. Garnett, A. Huijser, S. H. C. Askes, *Adv. Opt. Mater.* **2021**, *9*, 2100510.
[33] S. C. Nguyen, Q. Zhang, K. Manthiram, X. Ye, J. P. Lomont, C. B. Harris, H. Weller, A. P. Alivisatos, *ACS Nano* **2016**, *10*, 2144.
[34] W. M. Haynes (Editor), *CRC Handbook of Chemistry and Physics*, CRC Press, Boca Raton, Fla., 96th edition **2015**.
[35] M. Y. Razzaq, M. Anhalt, L. Frormann, B. Weidenfeller, *Mater. Sci. Eng. A* **2007**, *444*, 227.
[36] C. Zhan, X.-J. Chen, J. Yi, J.-F. Li, D.-Y. Wu, Z.-Q. Tian, *Nat. Chem. Rev.* **2018**, *2*, 216.
[37] A. W. Powell, A. Stavrinadis, I. de Miguel, G. Konstantatos, R. Quidant, *Nano Lett.* **2018**, *18*, 6660.
[38] Y.-S. Chen, W. Frey, S. Kim, K. Homan, P. Kruizinga, K. Sokolov, S. Emelianov, *Opt. Express* **2010**, *18*, 8867.
[39] W. Li, X. Chen, *Nanomedicine* **2015**, *10*, 299.
[40] L. Jauffred, A. Samadi, H. Klingberg, P. M. Bendix, L. B. Oddershede, *Chem. Rev.* **2019**, *119*, 8087.
[41] G. Baffou, H. Rigneault, *Phys. Rev. B* **2011**, *84*, 035415.
[42] J. Cunha, T.-L. Guo, G. Della Valle, A. N. Koya, R. Proietti Zaccaria, A. Alabastri, *Adv. Opt. Mater.* **2020**, *8*, 2001225.
[43] M. R. Gonçalves, *J. Phys. D* **2014**, *47*, 213001.
[44] G. Mie, *Ann. Phys.* **1908**, *330*, 377.
[45] P. B. Johnson, R. W. Christy, *Phys. Rev. B* **1972**, *6*, 4370.
[46] S. H. C. Askes, E. C. Garnett, *Adv. Mater.* **2021**, *33*, 2105192.
[47] S. M. Hatam-Lee, F. Jabbari, A. Rajabpour, *Nanoscale Microscale Thermophys. Eng.* **2022**, *26*, 40.
[48] A. Plech, V. Kotaidis, S. Grésillon, C. Dahmen, G. von Plessen, *Phys. Rev. B* **2004**, *70*, 195423.
[49] J. Park, J. Huang, W. Wang, C. J. Murphy, D. G. Cahill, *J. Phys. Chem. C* **2012**, *116*, 26335.
[50] P. A. Schoen, B. Michel, A. Curioni, D. Poulikakos, *Chem. Phys. Lett.* **2009**, *476*, 271.
[51] J. Park, D. G. Cahill, *J. Phys. Chem. C* **2016**, *120*, 2814.
[52] T. Hartman, B. M. Weckhuysen, *Chem. Eur. J.* **2018**, *24*, 3733.
[53] A. J. Schmidt, J. D. Alper, M. Chiesa, G. Chen, S. K. Das, K. Hamad-Schifferli, *J. Phys. Chem. C* **2008**, *112*, 13320.
[54] X. Wu, Y. Ni, J. Zhu, N. D. Burrows, C. J. Murphy, T. Dumitrica, X. Wang, *ACS Appl. Mater. Interfaces* **2016**, *8*, 10581.
[55] J. Huang, J. Park, W. Wang, C. J. Murphy, D. G. Cahill, *ACS Nano* **2013**, *7*, 589.
[56] M. Burzo, P. Komarov, P. Raad, *IEEE Trans. Compon. Packag. Technol.* **2003**, *26*, 80.
[57] R. Kato, I. Hatta, *Int. J. Thermophys.* **2008**, *29*, 2062.
[58] Z. Xu, D. Huang, T. Luo, *J. Phys. Chem. C* **2021**, *125*, 24115.
[59] M. Hu, X. Wang, G. V. Hartland, V. Salgueiriño-Maceira, L. M. Liz-Marzán, *Chem. Phys. Lett.* **2003**, *372*, 767.
[60] M. M. Coleman, K. H. Lee, D. J. Skrovanek, P. C. Painter, *Macromolecules* **1986**, *19*, 2149.
[61] C. P. Christenson, M. A. Harthcock, M. D. Meadows, H. L. Spell, W. L. Howard, M. W. Creswick, R. E. Guerra, R. B. Turner, *J. Polym. Sci. Part B* **1986**, *24*, 1401.
[62] L.-S. Teo, C.-Y. Chen, J.-F. Kuo, *Macromolecules* **1997**, *30*, 1793.
[63] X. Zhao, Y. H. Qi, K. J. Li, Z. P. Zhang, *Key Eng. Mater.* **2019**, *815*, 151.
[64] V. W. Srichatrapimuk, S. L. Cooper, *J. Macromol. Sci. Part B* **1978**, *15*, 267.
[65] T. Meng, Y. Sun, C. Tong, P. Zhang, D. Xu, J. Yang, P. Gu, J. Yang, Y. Zhao, *Nano Lett.* **2021**, *21*, 3843.
[66] H. Ying, Y. Zhang, J. Cheng, *Nat. Commun.* **2014**, *5*, 3218.
[67] G. Baffou, I. Bordacchini, A. Baldi, R. Quidant, *Light-Sci. Appl.* **2020**, *9*, 108.
[68] H. J. Sielcken, H. J. Bakker, *Phys. Rev. B* **2020**, *102*, 134301.
[69] J. Hohlfeld, S.-S. Wellershoff, J. Güdde, U. Conrad, V. Jähnke, E. Matthias, *Chem. Phys.* **2000**, *251*, 237.
[70] M. Hu, G. V. Hartland, *J. Phys. Chem. B* **2002**, *106*, 7029.
[71] M. Pastorczak, M. Nejbauer, C. Radzewicz, *Phys. Chem. Chem. Phys.* **2019**, *21*, 16895.
[72] S. Link, A. Furube, M. B. Mohamed, T. Asahi, H. Masuhara, M. A. El-Sayed, *J. Phys. Chem. B* **2002**, *106*, 945.
[73] Z. Ge, D. G. Cahill, P. V. Braun, *Phys. Rev. Lett.* **2006**, *96*, 186101.
[74] M. B. Mohamed, T. S. Ahmadi, S. Link, M. Braun, M. A. El-Sayed, *Chem. Phys. Lett.* **2001**, *343*, 55.
[75] E. L. Keller, H. Kang, C. L. Haynes, R. R. Frontiera, *ACS Appl. Mater. Interfaces* **2018**, *10*, 40577.
[76] J. Zhao, H. Su, G. E. Vansuch, Z. Liu, K. Salaita, R. B. Dyer, *ACS Nano* **2019**, *13*, 515.
[77] X. Ye, C. Zheng, J. Chen, Y. Gao, C. B. Murray, *Nano Lett.* **2013**, *13*, 765.
[78] C. A. Schneider, W. S. Rasband, K. W. Eliceiri, *Nat. Methods* **2012**, *9*, 671.
[79] P. Virtanen, R. Gommers, T. E. Oliphant, M. Haberland, T. Reddy, D. Cournapeau, E. Burovski, P. Peterson, W. Weckesser, J. Bright, S. J. van der Walt, M. Brett, J. Wilson, K. J. Millman, N. Mayorov, A. R. J. Nelson, E. Jones, R. Kern, E. Larson, C. J. Carey, İ. Polat, Y. Feng, E. W. Moore, J. Van der Plas, D. Laxalde, J. Perktold, R. Cimrman, I. Henriksen, E. A. Quintero, C. R. Harris, A. M. Archibald, A. H. Ribeiro, F. Pedregosa, P. van Mulbregt, *Nat. Methods* **2020**, *17*, 261.
[80] J. Wolberg, *Data Analysis Using the Method of Least Squares*, Springer-Verlag, Berlin/Heidelberg **2006**.
[81] Y. Hu, L. Zeng, A. J. Minnich, M. S. Dresselhaus, G. Chen, *Nat. Nanotechnol.* **2015**, *10*, 701.
[82] W. Zhu, G. Zheng, S. Cao, H. He, *Sci. Rep.* **2018**, *8*, 10537.
[83] X. Chen, A. Munjiza, K. Zhang, D. Wen, *J. Phys. Chem. C* **2014**, *118*, 1285.
[84] M. D. Losego, M. E. Grady, N. R. Sottos, D. G. Cahill, P. V. Braun, *Nat. Mater.* **2012**, *11*, 502.
[85] M. Hu, J. V. Goicochea, B. Michel, D. Poulikakos, *Appl. Phys. Lett.* **2009**, *95*, 151903.
[86] B. J. Sumlin, W. R. Heinson, R. K. Chakrabarty, *J. Quant. Spectrosc. Radiat. Transfer* **2018**, *205*, 127.
[87] L. F. Shampine, M. W. Reichelt, *SIAM J. Sci. Comput.* **1997**, *18*, 1.
[88] G. Baffou, P. Berto, E. Bermúdez Ureña, R. Quidant, S. Monneret, J. Polleux, H. Rigneault, *ACS Nano* **2013**, *7*, 6478.
[89] J. C. J. Mertens, B. Spitzbarth, R. Eelkema, J. Hunger, M. A. van der Veen, Dataset from "Predicting and Probing the Local Temperature Rise Around Plasmonic Core–Shell Nanoparticles to Study Thermally Activated Processes"; 4TU.R-esearchData, 2024; DOI: 10.4121/3d09872e-c111-4476-b339-30cc1f6557e8.

Manuscript received: February 15, 2024
Revised manuscript received: May 27, 2024
Accepted manuscript online: May 28, 2024
Version of record online: ■■, ■■

RESEARCH ARTICLE

Gold–silica core–shell nanoparticles can transform light into ultrafast temperature rises. We show computationally that they can heat the environment in tens of picoseconds in different media and we also show experimentally that high local temperatures can be reached on this timescale. This shows the potential of these nanoparticles as chemically inert nanoheaters to study thermally activated processes using pump–probe spectroscopy.

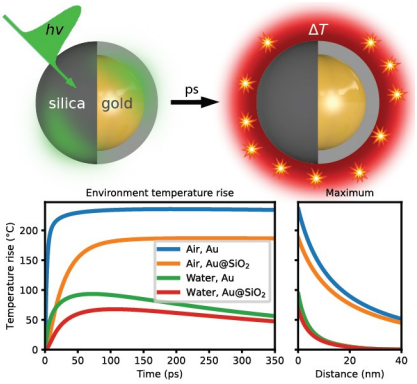

*J. C. J. Mertens, Dr. B. Spitzbarth, Dr. R. Eelkema, Dr. J. Hunger, Dr. M. A. van der Veen**